Adsorption of He isotopes on fluorographene and graphane: Fluid and superfluid phases from quantum Monte Carlo calculations

M. Nava,[1] D. E. Galli,[1] M. W. Cole,[2] and L. Reatto[1]

[1]*Dipartimento di Fisica, Università degli Studi di Milano, via Celoria 16, 20133 Milano, Italy*

[2]*Department of Physics, Penn State University, University Park, Pennsylvania 16802, USA*

(Received 24 April 2012; revised manuscript received 12 October 2012; published 8 November 2012)

Monolayer films on graphite, remarkably diverse examples of two-dimensional matter, are now well understood in terms of semiempirical interactions. We explore the phase behavior of helium films on two variants of graphene: graphane (graphene coated with H, denoted GH) and graphene fluoride (GF). The behaviors predicted with quantum Monte Carlo differ qualitatively from those on graphite because of the different surface composition, symmetry, and spacing of the adsorption sites. On both substrates we find that the analog of the standard $\sqrt{3} \times \sqrt{3}\ R30^\circ$ commensurate state on graphite is unstable. Results include a superfluid ground state for ^{4}He and a fluid ground state for ^{3}He, neither of which has been found for the monolayer film on any substrate; these two-dimensional fluids are anisotropic because of the symmetry imposed by the honeycomb lattice of adsorption sites. In the case of ^{4}He on GF the anisotropy is as large as if the superfluid were restricted to move in a multiconnected space, along the bonds of a honeycomb lattice. The superfluid transition temperature at the ground-state density of ^{4}He on GF (GH) is of order 0.25 (1.1) K. At higher coverages both an incommensurate triangular solid and a commensurate state at filling factor 2/7 are found.

DOI: 10.1103/PhysRevB.86.174509 PACS number(s): 67.25.bh, 02.70.Ss, 67.30.ej

I. INTRODUCTION

A focus of research in condensed matter physics is the study of strongly interacting systems, with a remarkable variety of phase transitions.[1] The effects of fluctuations are enhanced in low dimensions and in the presence of frustration.[2] These represent some of the motivations for studying adsorption phenomena, where important roles are played by the gas-gas interaction and the "tunable" effect of the substrate. The surface of graphite has long been a playground for studying two-dimensional (2D) monolayer phases of diverse gases.[3] The behavior depends sensitively on the commensurability, i.e., the relationship between the size parameter σ of the gas and the lattice constant of the surface. Among the simple gases, one encounters dramatic effects of the periodic potential for both isotopes of He and for H_2 (the smallest σ values). This corrugation leads to the existence, up to a relatively high order-disorder temperature T_{od} ($\sim$3 K for He and 20 K for H_2), of a $\sqrt{3} \times \sqrt{3}\ R30^\circ$ commensurate state on graphite. In striking contrast, Ar and CH_4 ($\sigma \sim 30\%$ greater than He and H_2) films are relatively well described by simple 2D models, in which the corrugation plays a *negligible* role. At high coverage a common feature of all of these gases is the presence of a solid phase, incommensurate with the substrate. In the second layer of ^{4}He on graphite some experiments have hinted at the presence of a supersolid phase.[4] When Fermi statistics are relevant, as in the case of ^{3}He, diverse many-body magnetic phenomena are also present.[5]

The recent interest in graphene (Gr) has led us to consider it as a logical substrate for adsorption studies. Since Gr is a single plane of graphite, the symmetry is identical and the corrugation is very similar in the two cases. If Gr is rigid, no new phenomena are expected for adsorption on one side of Gr, in comparison with graphite,[6] as has been verified by recent quantum simulations of ^{4}He.[7,8] The situation is different for the derivatives of Gr, graphene fluoride (GF),[9] also called fluorographene, and graphane (GH),[10] that have been recently obtained experimentally. Because GF and GH have surface symmetries and compositions which are quite different from Gr, adsorbed gases will have very different properties. This article presents results for adsorbed He isotopes, including both energy bands and monolayer phase behaviors. A major prediction for ^{4}He is that the analog of the standard $\sqrt{3} \times \sqrt{3}\ R30^\circ$ commensurate state is unstable on both GF and GH and that the ground state is a self-bound liquid that is superfluid and strongly modulated by the adsorption potential. A self-bound liquid is a state in which the energy per atom is less than that of a single atom. At larger coverage, both an incommensurate solid and a commensurate state at coverage $x = 2/7$ are found. We predict that ^{3}He on GF and GH at low coverage forms an anisotropic Fermi fluid and present evidence that on GF there might be found a *self-bound liquid* ^{3}He ground state (in contrast with the strictly 2D limit, for which a gas is the ground state[11]).

The structure of the paper is the following. In Sec. II we describe the geometry of the substrates and some characteristics of the adopted adsorption potential; in Sec. III we show our results for ^{4}He and ^{3}He one-body properties; Sec. IV contains the results for the many-body properties of the first ^{4}He layer on the substrates, ranging from low coverages to completion; in Sec. V we show our calculation for ^{3}He at low coverages; Sec. VI contains our conclusions. Appendix A contains the details of the adopted adsorption potential; Appendix B contains some computational details of the quantum Monte Carlo simulations.

II. GEOMETRY OF SUBSTRATES AND ADSORPTION POTENTIAL

In suspended GF (GH), half of the F (H) atoms are attached above the graphene sheet to C atoms forming one of the two sublattices of graphene and half are attached below to C atoms

of the other sublattice. With such a sandwich geometry a He atom approaching GF (GH) from above interacts primarily with the top F (H) overlayer, but only weakly with the C atoms and the F (H) atoms of the underlayer. Recently,[12] we developed a model adsorption potential $V_{\rm ad}(\vec{r})$ of a He atom at position $\vec{r}$ near these surfaces, adopting a traditional semiempirical model to construct the potential energy of a single He atom at position $\vec{r}$ near a surface.[13–15] The adopted adsorption potential for a He atom at position $\vec{r}$ above the substrate reads

$$V_{\rm ad}(\vec{r}) = v_{\rm rep}(\vec{r}) + v_{\rm att}(\vec{r}), \quad (1)$$

where the repulsive term $v_{\rm rep}(\vec{r}) = \gamma\rho(\vec{r})$ is proportional to the electron density of the substrate and the attractive part is a sum of the contributions of the different layers of the substrate. The atomic positions of GF (GH) and $\rho(\vec{r})$ come[12] from a density functional theory (DFT) computation with interaction parameters[12] taken from the literature (see Appendix A for details).

The F (H) atoms of the upper plane of GF (GH) form a triangular lattice; adsorption sites lie above the centers of each nearest-neighbor triplet of F (H) atoms of the upper plane [see Fig. 1(a)]. There is one site per C atom, twice as many sites as occur on Gr and graphite. These sites form a honeycomb

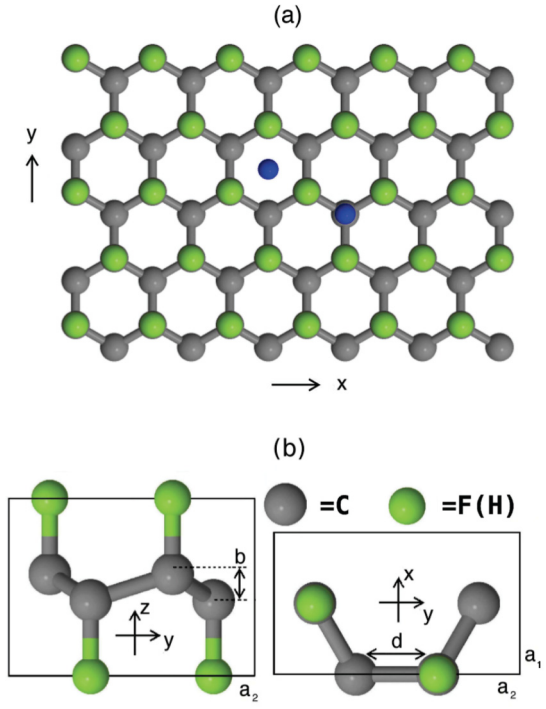

FIG. 1. (Color online) He on GF. (a) View of GF (GH) from above. Green circles represent F (H) atoms in the upper plane, dark gray circles represent half of the C atoms, and the other C atoms lie below the green circles. The other half of the F (H) atoms lie below the dark gray circles. The two blue circles represent two adsorption sites; one is on top of a C atom and the other has no atoms directly below. (b) Details of the geometry of the unit cell; a_1 and a_2 indicate the sides of the unit cell, d is the C-C distance projected on the x-y plane, and b is the buckling displacement of the C atoms. Values for a_1, a_2, d, and b have been obtained from a DFT computation (Ref. 12) and are reported in Appendix A.

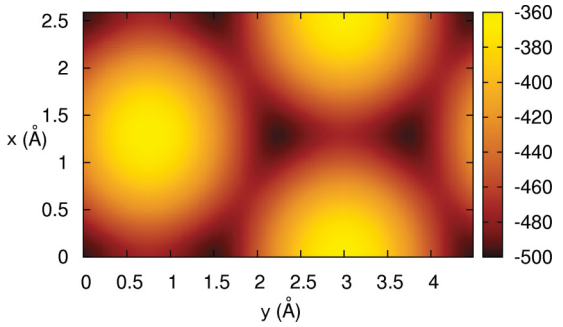

FIG. 2. (Color online) He on GF. Plot of the minimum value with respect to z of $V_{\rm ad}(\vec{r})$ in K as a function of x-y.

lattice; the two sites in the unit cell are not equivalent, as seen in Fig. 1(a), but the difference in adsorption energy between them is very small, <1% (see Fig. 2): On GF, the potential energy at the site which has no atoms directly below is about −496.467 K, to be compared with the potential energy at the other site which is about −496.122 K; both adsorption sites are located at $z = 3.6$ Å above the mean position of the C atoms. On GH, the potential energies which correspond to the same sites turn out to be about −195.015 K and −195.074 K, respectively, and the sites are located at $z = 3.7$ Å. Throughout this article we express energies in kelvins; this corresponds in showing the values obtained dividing the energies by the Boltzmann constant, k_B.

Figure 2 presents $V_{\rm ad}(\vec{r})$ for He GF. The depth of the potential well is about 496.5 (195) K for GF (GH) and the intersite energy barriers are 24 and 13 K, respectively. For comparison, on graphite the well depth is 224 K and the barrier is 41 K.[16] The potentials on GF and GH are remarkably different from those on graphite because of the different symmetry of the sites (honeycomb vs triangular) and the different energy parameters, and because the intersite distance (1.49 Å on GF, 1.45 Å on GH) is much smaller than on graphite (2.46 Å). On GF and GH $V_{\rm ad}(\vec{r})$ is characterized by narrow canyons between adsorption sites, with a relatively low energy barrier compared to graphite as shown in Fig. 3.

III. $N = 1$ ^{4}He AND ^{3}He PROPERTIES

We have computed[12] the exact ground state energy $\mathcal{E}_0$ of one ^{4}He and one ^{3}He atom on GF and GH with the path-integral ground state (PIGS) method.[17] See Appendix A for details on our computational method. Also, we computed the energy as a function of wave vector $\vec{k}$ in the lowest energy band from the imaginary time correlation function, $F(\vec{k},\tau) = \langle\hat{\rho}_{\vec{k}}(\tau)\hat{\rho}_{-\vec{k}}(0)\rangle$ ($\hat{\rho}_{\vec{k}}(\tau) = \exp[i\vec{k}\cdot\vec{r}(\tau)]$, where $\vec{r}$ is the position of the He atom), using powerful inversion methods: the genetic inversion via falsification of theories method[18] (GIFT). The results[12] for $\mathcal{E}_0$, the bandwidth of the lowest band, and the effective mass of ^{4}He on GF and GH are given in Table I. The ground-state energy $\mathcal{E}_0$ has a significant contribution from kinetic energy K: $K = 46.78(2)$ K on GF and $K = 20.51(1)$ K on GH. On graphite $K = 25.30(4)$ K when the Carlos-Cole adsorption potential is used.

The excited states of a He atom on a periodic potential are characterized by a series of energy bands as a function of wave

TABLE I. Left columns: Substrate and $N = 1$ properties. (U_o) Depth of potential well; (Δ) intersite energy barrier; (d_s) intersite distance; ($\mathcal{E}_0$) ground-state energy; (BW) bandwidth; (m^*/m) effective mass to bare mass ratio. Right columns: Many-body properties. ($\rho_{\rm eq}$) Equilibrium density; ($x_{\rm eq}$) coverage; (E_0) ground-state energy; ($E_b = \mathcal{E}_0 - E_0$) binding energy; $T = 0$ K condensate fraction (n_0) and superfluid fraction (ρ_s/ρ); (T_c) transition temperature; ($\rho_{I-\rm sat}$) first-layer completion density.

Substrate and $N = 1$ properties			Many-body properties		
Property	GF	GH	Property	GF	GH
U_0	496.5 K	195 K	$\rho_{\rm eq}$	0.049 Å^{-2}	0.042 Å^{-2}
Δ	24 K	13 K	$x_{\rm eq}$	0.142	0.115
d_s	1.49 Å	1.45 Å	E_0	−377.71(4) K	−134.02(5) K
$\mathcal{E}_0$ for ^{4}He	−376.16(2) K	−133.07(1) K	E_b	1.55(6) K	0.95(6) K
$\mathcal{E}_0$ for ^{3}He	−362.33(1) K	−126.97(2) K	n_0 ($T = 0$ K)	11 ± 1%	22.6 ± 1.3%
BW of ^{4}He	9.6 K	13.6 K	ρ_s/ρ ($T = 0$ K)	0.60(3)	0.95(3)
BW of ^{3}He	13.7 K	19.4 K	T_c	0.2–0.3 K	1.0–1.2 K
m^*/m of ^{4}He (^{3}He)	1.40 (1.26)	1.05 (1.01)	$\rho_{I-\rm sat}$	0.136 Å^{-2}	0.108 Å^{-2}

vector $\vec{k} = (k_x, k_y)$. In the case of He on graphite the lowest energy band[16] is separated from the next one by a gap. In the case of He on GF or GH, due to the honeycomb lattice, the first and the second bands should cross; i.e., the band gap should vanish, at the K and K′ points of the first Brillouin zone (BZ), the famous Dirac points.

The computed $F(\vec{k},\tau)$ is exact within the statistical errors, but the Laplace inversion is an ill-posed problem so the excited-state energy is affected by the uncertainty due to the inversion method. For each $\vec{k}$ the GIFT method is able to extract in a reliable way only the energy of one of the excited states, that state which has the strongest weight in the spectral function of the chosen correlation function, $F(\vec{k},\tau)$ in the present case, and this usually corresponds to the state of the lowest band. In Fig. 4 the computed energy bands for ^{3}He and ^{4}He on GF and GH are reported along two directions in reciprocal space. As seen in Table I, the effective mass enhancement on GF is much larger than that found on graphite ($m^\star/m = 1.06$ and 1.03 for ^{4}He and ^{3}He, respectively), while the enhancement on GH is similar to that on graphite.

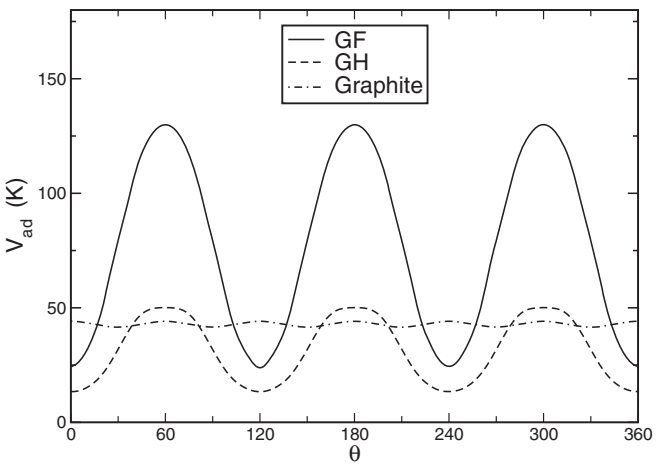

FIG. 3. Energy barrier in GF, GH, and graphite along a line at an angle θ with the horizontal direction, following the height $z(x,y)$ giving the minimum of $V_{\rm ad}(\vec{r})$. Plotted energy is relative to energy at the adsorption site.

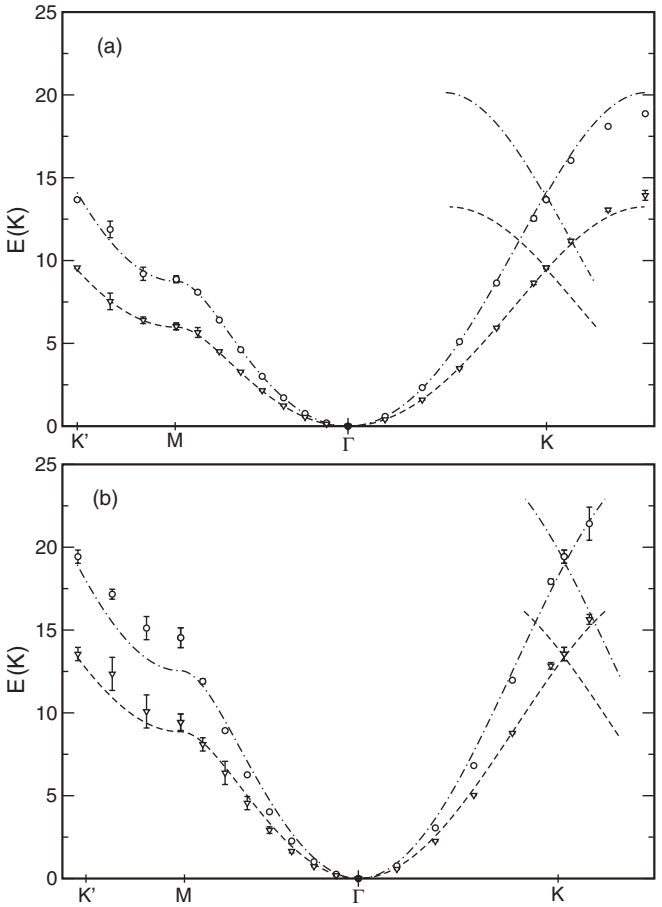

FIG. 4. (a) Energy of the first band along two directions of the first Brillouin zone for ^{4}He (triangles) and ^{3}He (circles) on GF. Data along ΓK beyond the Dirac point K give the results in the second Brillouin zone. The dashed lines are fits made with the tight-binding model on a honeycomb lattice with nearest-neighbor parameter $\gamma_1 = 3.63$ (5.695) for ^{4}He (^{3}He) and next-nearest-neighbor parameter $\gamma_2 = -0.16$ (−0.33). Close to the K point the second band given by the tight-binding model is also plotted in order to show the presence of the the Dirac point in the spectrum. (b) Same as for (a) for ^{4}He and ^{3}He on GH. The fit parameters for the dashed lines are $\gamma_1 = 4.514$ (6.434) for ^{4}He (^{3}He) and $\gamma_2 = -0.021$ (−0.04). More information can be found in Ref. 12.

IV. RESULTS FOR FIRST ^{4}He ADSORBED LAYER ON GF AND GH

A. Low-coverage regime

With the PIGS method we computed the exact ground state properties of N ^{4}He atoms on GF and GH as a function of the density, ρ. As interatomic potential we used an Aziz potential[19] and $10 < N < 200$, with a number of unit cells which ranges between 12×5 and 24×12.

The ground state of ^{4}He in mathematical 2D is a self-bound superfluid at density $\rho_{\rm eq} = 0.044$ Å^{-2} and energy per atom $E_0 = -0.84$ K.[20] In the 3D model of an x-y translationally invariant potential with z dependence appropriate for ^{4}He/graphite, the ground-state values are similar: $\rho_{\rm eq} = 0.044$ Å^{-2} and $E_0 = -0.91$ K[21] relative to the single atom's energy. When the corrugation of the graphite adsorption potential is turned on, the superfluid state is suppressed; the atoms localize in a nonsuperfluid commensurate solid (CS) phase, with $\sqrt{3} \times \sqrt{3}\,R30^\circ$ order. They occupy second-nearest–neighbor sites, separated by 4.26 Å, with $x = 1/3$ as the filling fraction of the adsorption sites.[22] This agrees with experiment.[3] A commensurate state *similar* to the $\sqrt{3} \times \sqrt{3}$ $R30^\circ$ on graphite could, *in principle*, be present also on GF and GH; such a state corresponds to a filling factor $x = 1/6$ ($\rho = 0.0573$ Å^{-2} on GF and $\rho = 0.0608$ Å^{-2} on GH, different due to lattice expansions relative to Gr), with fifth-neighbor sites occupied. A simple consideration suggests the instability of a similar commensurate state. Using the curvature of the He-substrate potential at an adsorption site, the 2D zero point energy is estimated to be 55 (40) K on GF (GH), much larger than the minimum potential barrier 23 (13) K, so that such a localized state should be unstable. This is indeed what we find with a many-body computation. At $x = 1/6$ starting the simulation from an ordered configuration, after a short Monte Carlo evolution the system becomes disordered, as seen in the static structure factor $S(k)$ of Fig. 5 for ^{4}He on GF. It displays only those Bragg peaks, i.e., sharp peaks that scale as N, with the periodicity of the substrate potential, while no peaks corresponding to occupation of fifth neighbors are present. At $k \simeq 1.8$ Å broad peaks, independent of N, appear representing *anisotropic* short-range order. The same behavior is found for ^{4}He on GH.

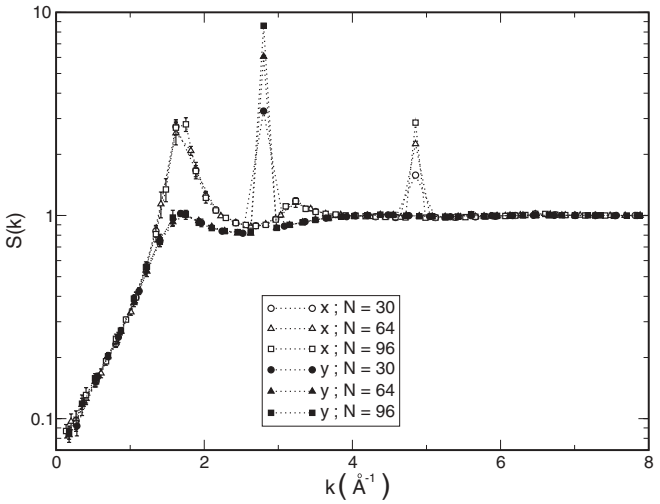

FIG. 5. $S(k)$ of ^{4}He on GF in the k_x or (1,0) and k_y or (0,1) directions at coverage $x = 1/6$ for indicated numbers of particles. Notice the logarithmic scale for $S(k)$. The dotted lines represent a guide to the eye.

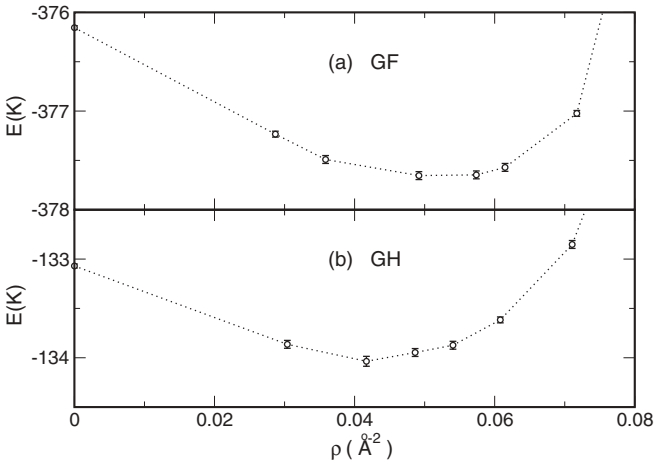

FIG. 6. (a) Energy per particle of ^{4}He as function of the density ρ on GF at $T = 0$ K. (b) Same as for (a) for ^{4}He on GH. In both cases, the used particle numbers ranged between $N = 60$ and $N = 120$. The dotted line represents a guide to the eye.

In Fig. 6 the energy per particle of ^{4}He on GF and ^{4}He on GH is reported. In both the cases a liquid phase has been found at least for densities up to filling factors $x = 1/4$, which for the GF case correspond to a density $\rho_{1/4}^{GF} = 0.0861$ Å^{-2}, and for the GH case to a density $\rho_{1/4}^{GH} = 0.0912$ Å^{-2}.

The equilibrium density for ^{4}He on GF is $\rho_{\rm eq}^{GF} = 0.049(1)$ Å^{-2} with a binding energy of 1.55(6) K; for ^{4}He on GH we found a self-bound state at equilibrium density $\rho_{\rm eq}^{GH} = 0.042(1)$ Å^{-2} with a binding energy of 0.95(6) K. In both cases, E_0 is below the adsorption energy of a single ^{4}He atom, meaning that the ground state is a self-bound liquid, strongly modulated by the substrate potential; in the GF case the cohesive energy is almost twice its 2D value (0.84 K). A manifestation of the strong anisotropy in the GF case is seen in Fig. 8(a) [plot of $S(k)$ in the (k_x,k_y) plane] and of Fig. 7 (plot of the local density as function of x-y); this ground state is superfluid, with a condensate fraction $n_0 = 11 \pm 1\%$ (see Fig. 9).

In Fig. 8(b) the static structure factor of ^{4}He on GH in the (k_x,k_y) plane at equilibrium density is shown. The sharp peaks reflect the density modulation due to the corrugation of the adsorption potential. The crater-like structure at smaller k represents short-range He-He correlations. It can be noticed that short-range correlations are much less anisotropic than that in the GF case [see Fig. 8(a)]; this reflects the smaller corrugation of the adsorption potential of GH.

B. Bose-Einstein condensate and superfluid density

As discussed above, at coverage $x = 1/6$ ^{4}He on GF and GH is not a commensurate solid but it is a fluid. Actually, it is a modulated superfluid as shown by the exact off-diagonal one body density matrix ρ_1 computed with PIGS (see Appendix B).

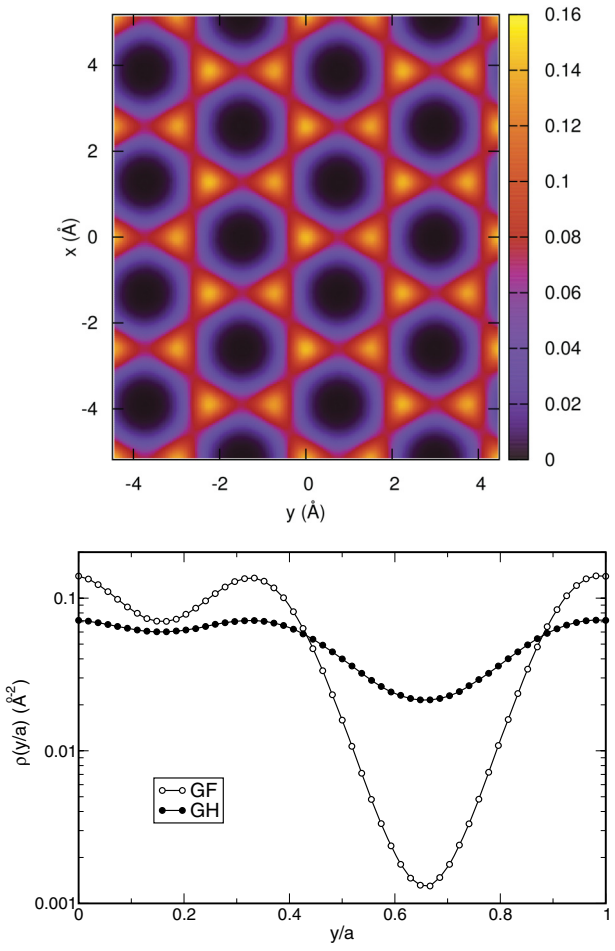

FIG. 7. (Color online) Upper panel: Local density $\rho(x,y)$ (in units of Å^{-2}) as function of x-y for ^{4}He at equilibrium density on GF. Lower panel: Local density $\rho(x=0,y)$ (in units of Å^{-2}) in the unit cell (with side $a = 4.486$ Å in the GF case and $a = 4.347$ Å in the GH case) along the y direction for ^{4}He at equilibrium density on GF and GH; note the logarithmic scale used for $\rho(x=0,y)$. Error bars are below the symbol size; lines are guides to the eye.

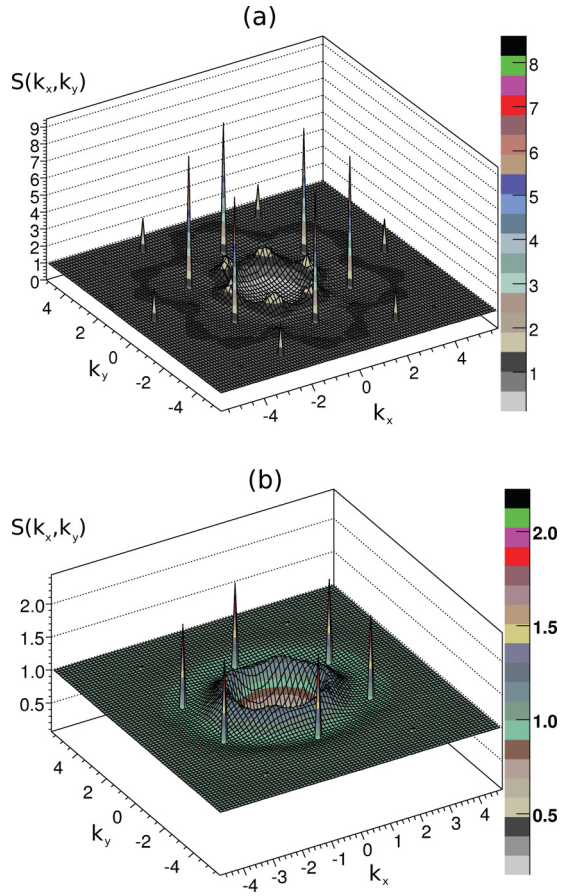

FIG. 8. (Color online) (a) Static structure factor, $S(k_x,k_y)$, at equilibrium density on the k_x-k_y plane for $N = 96$ atoms of ^{4}He on GF. (b) The same for ^{4}He on GH at equilibrium density. k_x and k_y axis are expressed in Å^{-1}. These static structure factors are characteristic of a modulated liquid; sharp peaks represent the first two stars of Bragg peaks due to the substrate, while the broad peaks indicate *anisotropic* short-range order.

ρ_1 has a plateau at large r (see Fig. 9) corresponding to a Bose-Einstein condensate (BEC) fraction $n_0 = 7.3 \pm 1.5\%$ for ^{4}He on both GF and GH. A larger value of the condensate is present at the equilibrium density, 11 ± 1 % on GF and $22.6 \pm 1.3\%$ on GH. Some of the ground-state properties are given in Table I for both substrates.

A quantity of major interest is the superfluid fraction ρ_s/ρ. Notice that also the value of ρ_s/ρ at $T = 0$ K is of great interest because this quantity is less than unity in a nonuniform superfluid, as predicted by Leggett.[23] We computed the superfluid fraction ρ_s/ρ at $T = 0$ K from the diffusion coefficient of the center of mass $\vec{R}_{CM}(\tau)$ in imaginary time[24] with PIGS:

$$\frac{\rho_s}{\rho} = \lim_{\tau\to\infty} D_s(\tau),$$
$$D_s(\tau) = \frac{N}{4\lambda}\frac{\langle[\vec{R}_{CM}(\tau) - \vec{R}_{CM}(0)]^2\rangle}{\tau}, \quad (2)$$

where the squared distance $[\vec{R}_{CM}(\tau) - \vec{R}_{CM}(0)]$ is evaluated without invoking periodic boundary conditions, i.e., including boundary crossing if $\vec{R}_{CM}(\tau)$ leaves the main simulation box. At $T \neq 0$ the superfluid fraction has been computed from the winding numbers given by path-integral Monte Carlo (PIMC)[25] simulations. In Fig. 10 the superfluid fraction ρ_s/ρ is shown in function of the temperature for a system of $N = 26$ atoms of ^{4}He on GF and $N = 20$ atoms of ^{4}He on GH at their respective equilibrium densities. It is noticeable that ρ_s/ρ for ^{4}He on GH at the lowest T joins smoothly with the $T = 0$ K value. This is a strong test on our algorithms since these values come from completely different computations. In the case of GF, the low transition temperature does not allow us to reach the $T \ll T_c$ regime. At $T = 0$ K, for ^{4}He on GF we obtain $\rho_s/\rho = 0.60(3)$ and $\rho_s/\rho = 0.95(3)$ on GH. From ρ_s/ρ at finite T and taking into account how size effects affect the superfluid fraction, we estimate the superfluid transition temperature $T_c \simeq 0.2$–0.3 K for GF and $T_c \simeq 1.0$–1.2 K on GH. These values should be taken with some caution because the number of particles in our computations is rather small so that a significant size effect could be present. It should be noticed that the present

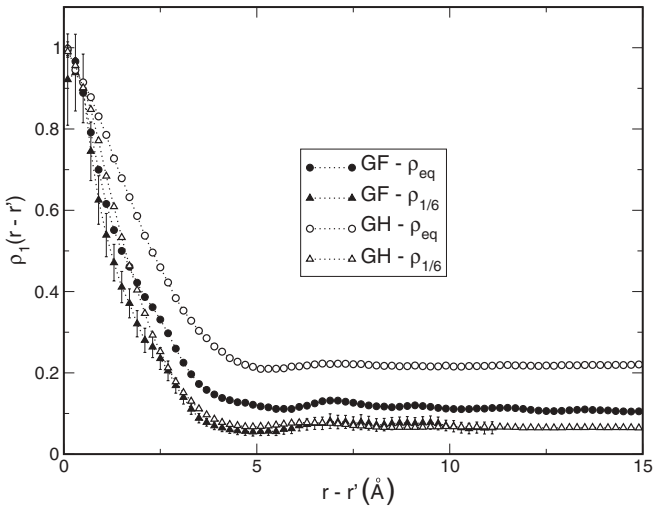

FIG. 9. Off-diagonal density matrix $\rho_1(r)$ on GF and GH at $\rho_{1/6}$ and at $\rho_{\rm eq}$.

QMC computations are very demanding due to the very strong adsorption potential with large corrugation. For this reason we have not attempted a careful study of size effects so that our results are semiquantitative for an infinite system.

In conclusion, we predict that a submonolayer ^{4}He film on GF (GH) is an *anisotropic* superfluid up to 0.2–0.3 K (1.0–1.2 K); this represents a long-sought phase, found so far only with trapped cold atoms.[26]

C. High coverages

We have studied the stability of two other hypothetical commensurate phases on GF and GH. At coverage $x = 1/4$ (corresponding to occupying sites that are third-nearest neighbors) we find that the ordered state is unstable.

At coverage $x = 2/7$ it is possible to put the He atoms in a triangular lattice with 1/3 of the atoms located at adsorption sites. At this coverage, which corresponds to $\rho = 0.0984$ Å^{-2}

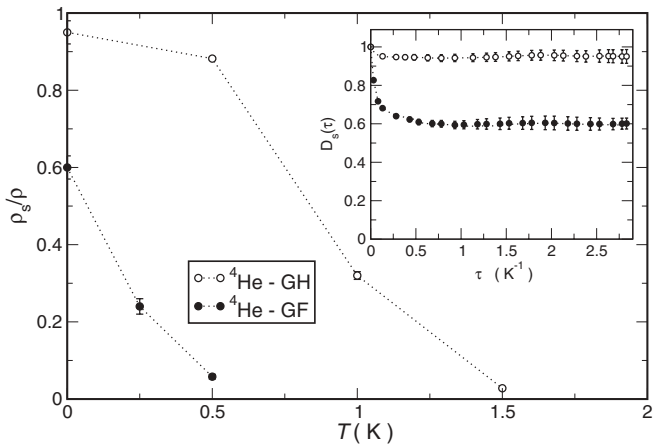

FIG. 10. The superfluid fraction ρ_s/ρ at $\rho_{\rm eq}$ as function of temperature for a system of $N = 20$ atoms of ^{4}He on GH and a system of $N = 26$ atoms of ^{4}He on GF. The transition temperature can be roughly estimated in the range 1.0–1.2 K for ^{4}He GH and 0.2–0.3 K for ^{4}He GF. In the inset the superfluid fraction can be read as the long-τ limit of Eq. (2).

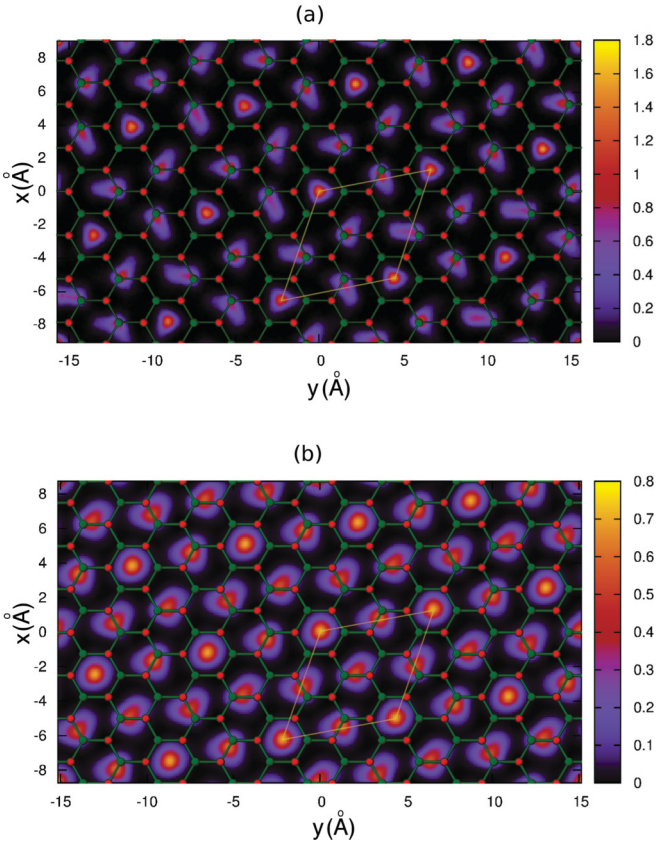

FIG. 11. (Color online) Local density (in Å^{-2} units) on the x-y plane of the 2/7 phase of ^{4}He on GF (a) and on GH (b) compared with the geometry of the substrate. Small red balls are centered on the position of fluorine atoms and the small green ones on the carbon atoms. Thin white lines enclose the unit cell of the commensurate 2/7 phase.

on GF and $\rho = 0.105$ Å^{-2} on GH, on both substrates we find that a commensurate triangular solid is stable, or at least metastable, containing 4 atoms in the unit cell of the triangular lattice rotated by 19.1° with respect to the substrate potential. In the unit cell one of the ^{4}He atoms is localized on an adsorption site in the middle of a graphene hexagonal ring, two other atoms approach adsorption sites of the other kind, and finally the fourth one is centered on a saddle point of the potential. This state has some similarity with the 4/7 commensurate state found for ^{3}He in the second layer on graphite[5] preplated by one ^{4}He layer. The local densities Fig. 11(a) for ^{4}He on GF and Fig. 11(b) on GH manifest the presence of a superlattice with four atoms in the unit cell of the triangular lattice.

The static structure factors, $S(k_x,k_y)$ (see Fig. 12), have prominent Bragg peaks forming three stars. The star of the six highest peaks is the main Bragg peaks of a triangular lattice with lattice parameter equal to that of a triangular lattice at this density. Another star represents the density modulation due to the adsorption potential. The third star formed by six less intense peaks at a smaller wave vector is a combination of vectors of the two previous stars, thus corresponding to interference between the triangular and the honeycomb modulation. The intensities of all these peaks scale

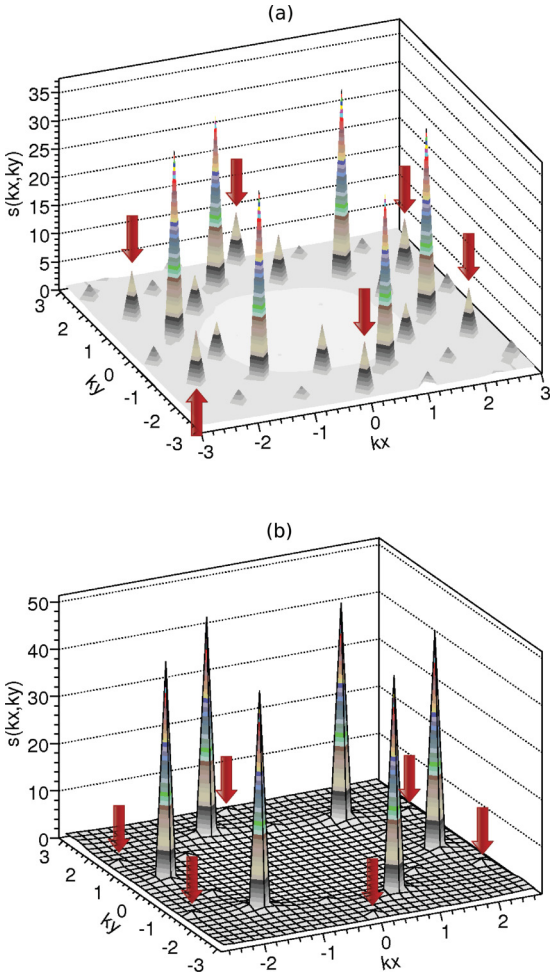

FIG. 12. (Color online) Static structure factor on the k_x-k_y plane of the 2/7 phase of $N = 112$ atoms of ^{4}He on GF (a) and on GH (b). k_x and k_y axes are expressed in Å^{-1}. Red arrows point to the peaks corresponding to the density modulation imposed by the adsorption potential.

with the number of particles (data not shown). Additional peaks are present reflecting the superlattice but these peaks are very weak and hardly visible in the figure. It can be noticed that the much smaller intensity of the Bragg peaks is due to the adsorption potential in the case of GH as can be expected due to the weaker corrugation of the adsorption potential of GH.

At large coverage at densities in the neighborhood of this 2/7 phase we find an incommensurate triangular state, which is strongly deformed by the substrate potential. The local stability of the three phases, modulated liquid, 2/7 commensurate triangular solid, and incommensurate triangular solid, is shown in the equation of state in Fig. 13 by the different symbols. It should be noticed that this is not a true phase diagram because we have not studied the possibility of coexistence of phases.

We have estimated the first layer's completion density, $\rho_{I-\mathrm{sat}}$ (results in Table I), by increasing N until some atoms spill out of the first layer and the density profile in the direction normal to the surface develops two well-separated peaks. The promotion to the second layer takes place at a density ρ_{sat}^{GF} =0.136 Å^{-2} for the GF case and a density ρ_{sat}^{GH} =0.108 Å^{-2} for the GH case. Beyond such densities, the

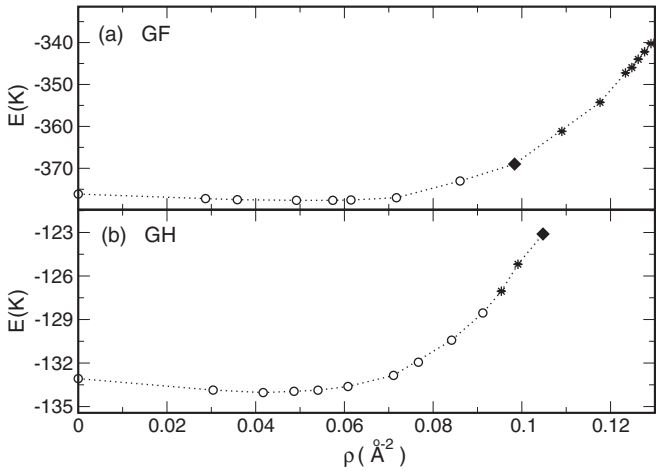

FIG. 13. (a) Energy per particle of ^{4}He as function of the density ρ on GF at $T = 0$ K. (b) Same as for (a) for ^{4}He on GH. The filled diamonds mark the energy of the 2/7 phase on both substrates; the stars represent the energies of incommensurate phases before completion. The dashed line represents a guide to the eye.

occupation of the second layer is clearly visible as a secondary peak in the local density along the z direction (Fig. 14). We note that the monolayer completion density on graphite is 0.12 atoms per Å^2, intermediate between the values found here for GF and GH.

A systematic search for other possible commensurate phases for densities between ρ_{eq} and $\rho_{I-\mathrm{sat}}$ and a study of phase coexistence at large coverage remain to be done. In the GF case we have investigated the density range between $\rho_{2/7}^{GF} = 0.0984$ Å^{-2} and $\rho_{\mathrm{sat}}^{GF} = 0.136$ Å^{-2} and as an example $S(k_x,k_y)$ at $\rho = 0.123$ Å^{-2} is shown in Fig. 15. As initial configuration we have used a disordered one as well as an ordered triangular configuration. The runs converge to the same results: $S(k_x,k_y)$ is dominated by a star of six peaks as expected for a triangular solid. The wave vectors of these peaks are not exactly equal to the value of an ideal triangular solid at this density implying

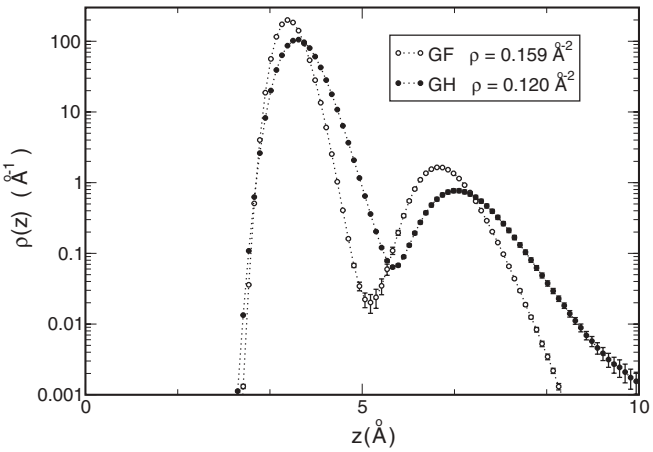

FIG. 14. Local density along the z direction of ^{4}He on GF (with $N = 111$) and ^{4}He on GH (with $N = 79$) at a density beyond the promotion density. The occupations of the first and the second layers are clearly visible as two peaks. The area under the peaks represents the number of ^{4}He atoms in the corresponding layer.

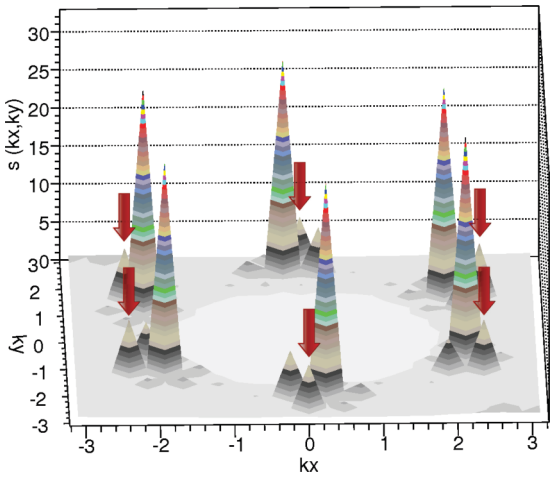

FIG. 15. (Color online) Static structure factor on the k_x-k_y plane of the incommensurate solid phase of $N = 86$ atoms of ^{4}He on GF at density $\rho = 0.123$ Å^{-2}. k_x and k_y axis are expressed in Å^{-1}. Red arrows point to the peaks corresponding to the density modulation imposed by the adsorption potential.

that the triangular order is deformed in order to better fit within the simulation box. $S(k_x,k_y)$ has additional Bragg peaks corresponding to the modulation of the substrate potential and to the interference between the previous two sets of peaks. Additional smaller peaks are present presumably as consequence of the presence of defects. The modulus of the main Bragg peaks increases in a smooth way as the density is increased as expected for an incommensurate triangular solid. The observed deviations from the value $k_B = 4\pi(\rho/2\sqrt{3})^{1/2}$ of an ideal triangular solid are explained by the deformations of the lattice and by the presence of some defects, mainly dislocations, that can be observed from the configuration of the atoms (data not shown).

In the case of GH we have investigated the density range 0.0916 Å^{-2} to $\rho_{2/7}^{GH} = 0.105$ Å^{-2}. Here, too $S(k_x,k_y)$ is dominated by the Bragg peaks of a triangular lattice [see Fig. 16

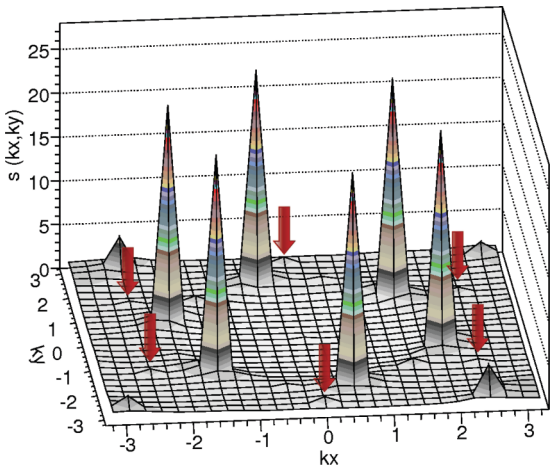

FIG. 16. (Color online) Static structure factor on the k_x-k_y plane of the incommensurate solid phase of $N = 66$ atoms of ^{4}He on GH at density $\rho = 0.102$ Å^{-2}. k_x and k_y axes are expressed in Å^{-1}. Red arrows point to the peaks corresponding to the density modulation imposed by the adsorption potential.

for $S(k)$ at density $\rho = 0.102$ Å^{-2}] that is incommensurate with respect to the substrate periodicity. The six peaks that in Figs. 12, 15, and 16 are marked by the red arrows represent the density modulation induced by the adsorption potential like the peaks in Fig. 8. The third set of peaks is merely an interference pattern of the first two sets.

V. ^{3}He ON GF AND GH AT LOW COVERAGE

The ground state of ^{3}He on graphite is the $\sqrt{3} \times \sqrt{3}\,R30°$ state. We expect that the analogous commensurate state on GF and GH is unstable, as for ^{4}He, because the smaller mass makes ^{3}He localization more expensive. Indeed, we have verified that this commensurate state for a mass 3 boson system is unstable toward a fluid state on both substrates. We determined the Fermi-Bose gap with a recently proposed method[27,28] based on the computation of the imaginary time correlation function of a Slater determinant. Given a specific Hamiltonian, this technique extracts the energy gap between the symmetric and antisymmetric ground state from a suitable fermionic imaginary-time correlation function computed as an exact average on the Bose ground state:

$$\mathcal{C}_F(\tau) \equiv \frac{\langle \psi_0^B | (e^{\tau \hat{H}} \hat{\mathcal{A}}_F^\dagger e^{-\tau \hat{H}}) \hat{\mathcal{A}}_F \psi_0^B \rangle_{\mathcal{H}(N)}}{\langle \psi_0^B | \psi_0^B \rangle_{\mathcal{H}(N)}}, \quad \tau \geqslant 0, \qquad (3)$$

where $\hat{\mathcal{A}}_F$ is, typically, a Slater determinant. The lowest energy contribution in $\mathcal{C}_F(\tau)$ yields the *exact gap* between the fermionic and the bosonic ground states, provided that one is able to obtain the inverse Laplace transform of $\mathcal{C}_F(\tau)$; this can be readily seen by formally expressing (3) on the basis $\{\psi_n^F\}_{n\geqslant 0}$ of eigenvectors of $\hat{H}$ corresponding to the eigenvalues $\{E_n^F\}_{n\geqslant 0}$:

$$\mathcal{C}_F(\tau) = \sum_{n=0}^{+\infty} e^{-\tau(E_n^F - E_0^B)} \frac{\left| \langle \hat{\mathcal{A}}_F \psi_0^B | \psi_n^F \rangle_{\mathcal{H}(N)} \right|^2}{\langle \psi_0^B | \psi_0^B \rangle_{\mathcal{H}(N)}}. \qquad (4)$$

We have shown that the inverse Laplace transform of $\mathcal{C}_F(\tau)$ can be handled efficiently with statistical inversion procedures, like the GIFT algorithm.[18,29] The Fermi-Bose gap $E_0^F - E_0^B$ is an extensive quantity, so this method in practice can be applied provided that the system is not too large.

The ground-state energies as function of density of mass 3 bosons and of the fermionic ^{3}He on GF and on GH are plotted in Fig. 17 as function of density; the gap $E_0^F - E_0^B$ is a smooth function of ρ and the energy at the density corresponding to the $\sqrt{3} \times \sqrt{3}$ state is well above the energy at lower densities implying that this ordered commensurate state is indeed unstable and the system is in a fluid state. In the figure we plot also the ^{3}He energy based on the crude approximation of taking as Fermi-Bose gap the kinetic energy $K_{\text{free}} = \hbar^2\pi\rho/2m^*$ of free fermions, where m^* is the effective mass of a ^{3}He atom on the substrate ($m^*/m = 1.26$ for GF, $m^*/m = 1.01$ for GH). For mass 3 bosons we find a bound state with a binding energy $E_0 = -0.22$ K at density $\rho_{\text{eq}} = 0.03$ Å^{-2}. Adding to the boson energy the Fermi-Bose gap the energy yields a shallow minimum in the density range 0.015–0.025 Å^{-2}, with a value equal within the statistical error to the energy of a single adsorbed ^{3}He on GF. Hence, the existence of a self-bound state on GF is an unresolved possibility.

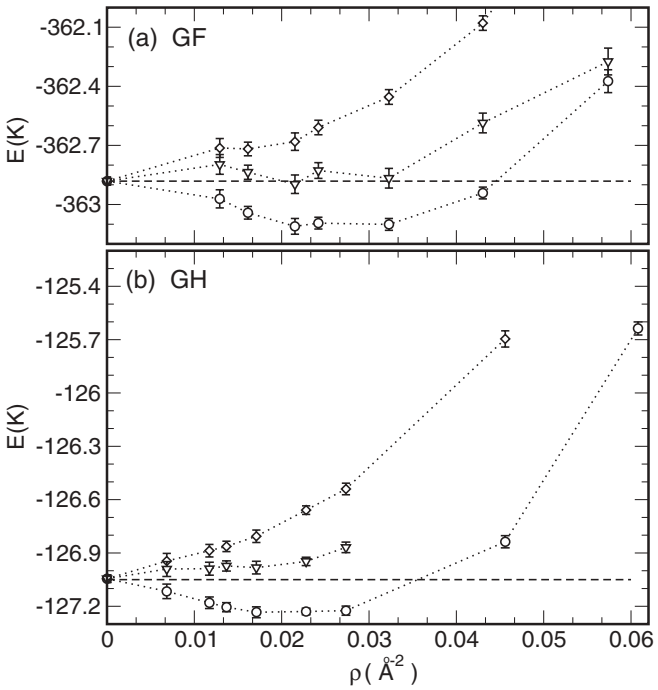

FIG. 17. (a) Ground-state energy as a function of density of mass 3 bosons on GF (circles), fermionic ^{3}He GF obtained via the fermionic correlations method (triangles), and fermionic ^{3}He GF obtained by approximating the Bose-Fermi gap with the kinetic energy of the free fermion gas (diamonds). (b) Same as for (a) for ^{3}He on GH. In both cases, the system under study was composed of $N = 18$ atoms of ^{3}He.

In conclusion, we predict the existence of two *anisotropic* Fermi fluids, in the sense that the local density is nonuniform and anisotropic, with a tunable density depending on the ^{3}He coverage. The density range depends on whether the ^{3}He atoms form a self-bound state. Our computations indicate that a self-bound liquid state is not present for ^{3}He on GH but it might be present on GF.

VI. CONCLUSIONS

In summary, our exploration of adsorbed ^{4}He and ^{3}He on the graphene derivatives, GF and GH, has been very rewarding. The corrugation of the adsorption potential is characterized by a much larger anisotropy around an adsorption site than on graphite and by a much smaller intersite distance. As a consequence, the predicted monolayer phase diagram is very different from that on graphite. The commensurate state analogous to the $\sqrt{3} \times \sqrt{3}$ $R30^\circ$ on graphite turns out to be unstable. In the case of ^{4}He the ground state is a self-bound superfluid with $\rho_s/\rho = 0.60$ and BEC fraction $n_0 = 11\%$ on GF and $\rho_s/\rho = 0.95$ and $n_0 = 23\%$ on GH. The superfluid transition temperature is about 0.25 K on GF and 1.1 K on GH. On both substrates the superfluid is nonuniform, with a honeycomb symmetry imposed by the adsorption potential. In the case of GF such nonuniformity is so extreme (the ^{4}He density above a F atom is one hundredth of the density at the adsorption site) as if the superfluid were restricted to move in a multiconnected space, along the bonds of a honeycomb lattice. At coverage close to completion of the first layer on both substrates we find an incommensurate triangular solid and, in addition, a commensurate triangular solid at coverage 2/7 of the adsorption sites. In both states the ^{4}He atoms are rather mobile, so these are good candidates for supersolidity. The study of this possibility is beyond the scope of the present paper. ^{3}He atoms on GF and GH at low coverage form a fluid so this offers the possibility of studying an anisotropic Fermi fluid, possibly superfluid at low temperatures.

We notice that the qualitative results presented here do *not* depend on the precise values of parameters entering the model adsorption potential. We have modified the less certain parameters by up to 20%, finding only quantitative changes, without modifying the qualitative aspects. Notice that in the case of GF our predictions are insensitive to the presence of regions of unreacted graphene by fluorine atoms as long as such regions leave a percolating GF substrate. In fact the twice greater adsorption energy on GF, compared to graphite, guarantees that the He atoms are preferentially adsorbed on the GF regions. Measurement of thermodynamic properties and He beam scattering experiment from GF and GH will provide sensitive tests of the accuracy of our model potential. We have predicted a number of phenomena for the He atoms on GF and GH that are quite different from those on any other known substrate and this calls for experimental verification. From the theoretical point of view many extensions of the present computations can be foreseen, e.g., study of the collective mode spectrum[30] of ^{4}He or the system under rotation. In the case of ^{3}He a full microscopic study of this nonuniform Fermi system has yet to be done. We have developed a model adsorption potential also for molecular hydrogen.[12] It will be very interesting to study the phase diagram of para-H_2 on GF.

ACKNOWLEDGMENTS

We wish to thank Jorge Sofo for discussion and for providing the charge density of GF and GH and Chris Billman for help in the early stages of this project, and also NSF for its support. This work has been supported by Regione Lombardia and CILEA Consortium through a LISA Initiative (Laboratory for Interdisciplinary Advanced Simulation) 2010 grant (http://lisa.cilea.it).

APPENDIX A: ADSORPTION POTENTIAL DETAILS

The geometry of GH and GF, their electronic charge density, and the electrostatic potential have been obtained[12] using DFT. As a result of the DFT calculation, the C-F distance is 1.38 Å, the C-C distance is 1.57 Å, the C-C distance projected on the x-y plane is $d = 1.495$ Å, and the buckling displacement $b = 0.484$ Å; while in GH, the C-H distance is 1.11 Å, the C-C distance 1.52 Å, $d = 1.453$ Å, and $b = 0.45$ Å [see Fig. 1(b)].

In the case of graphene fluoride (GF) we have

$$v_{\rm att}(\vec{r}) = v_{\rm F^+}(\vec{r}) + v_{gr}(\vec{r}) + v_{\rm F^-}(\vec{r}). \tag{A1}$$

The first term on the right-hand side of Eq. (A1) is the van der Waals (vdW) interaction between the helium atom and the fluorine *overlayer* atoms damped at small distances with the

TABLE II. Parameters for the adsorption potential of He on GH and GF.

Parameter	Value	Type
C_{6F}	4.2 eV Å^6	GF
C_{6H}	1.206 eV Å^6	GH
C_{6C}	3.447 eV Å^6	GF/GH
A_F	1.1 eV Å^4	GF
A_H	0.3455 eV Å^4	GH
β_F	3.2125 Å^{-1}	GF
β_H	3.77945 Å^{-1}	GH
γ	53.9392 eVÅ^3	GF/GH

Tang-Toennies procedure[15]

$$v_{F^+}(\vec{r}) = C_{6F} \sum_j \frac{1 - e^{(\beta_F \vec{x}_j)} \sum_{i=0}^{6} \frac{(\beta_F x_j)^i}{i!}}{x_j^6}, \tag{A2}$$

where $x_j = |\vec{r} - \vec{r}_j|$ and $\vec{r}_j$ is the position of the jth fluorine atom in the overlayer of the substrate. The v_{F^-} term is the interaction with the fluorine *underlayer* atoms; such atoms are far from the helium atoms so that this contribution has been integrated over the positions of the F^- atoms giving

$$v_{F^-}(\vec{r}) = -\frac{A_F}{z^4}, \tag{A3}$$

where z is the distance of the He atom at $\vec{r}$ from the fluorine underlayer. The remaining term v_{gr} is the vdW interaction of He with the graphene sheet; this has been considered as

$$v_{gr}(\vec{r}) = -C_{6C} \sum_j \frac{1}{x_j^6} \tag{A4}$$

with the sum running over the positions of the carbon atoms. We have also considered the induced electric dipole energy $U_{pol}(\vec{r}) = -\frac{\alpha_{He} E^2(\vec{r})}{2}$ where $\alpha_{He} = 0.205$ Å^3 is the static polarizability of the He atom and $\vec{E}(\vec{r})$ is the electric field due to the substrate. We have verified that this contribution is below 1% of $v_{att}(\vec{r})$ so that it is safely negligible.[12] The adopted parameters are shown in Table II. The less certain parameters are $\beta_{F(H)}$ and $C_{6F(H)}$; the robustness of the results of the present work have thus been checked against variation up to ±20% of these two parameters.

APPENDIX B: COMPUTATIONAL DETAILS

For the zero-temperature simulations we used the path-integral ground state (PIGS) method[17] with an eight-order multiple product expansion[31] of the propagator. The PIGS method can compute quantum averages of the ground state of the system using the quantum evolution in imaginary time τ of a trial wave function Ψ_t. If Ψ_t is not orthogonal to the ground state Ψ_0, and τ is large enough, the quantum evolution removes from Ψ_t the contributions of the excited states allowing the sampling of the configurations of the system on its ground state.

$$\Psi_0(R) \propto \lim_{\tau/2 \to \infty} \int dR'\, G\left(R, R', \frac{\tau}{2}\right) \Psi_t(R'), \tag{B1}$$

where R and R' are many-body coordinates (i.e., $R = \{\vec{r}_i\}_{i=1}^N$). The propagator $G(R, R', \frac{\tau}{2})$ is in general unknown but valid approximations can be obtained in the limit of small imaginary times. The propagator is thus exactly expressed as a convolution of $M/2$ propagators $G(R_i, R_{i+1}, d\tau)$ where $d\tau = \frac{\tau}{M}$. The configurations of the system are thus sampled from the following probability distribution:

$$p(R_0, \ldots, R_M) = \frac{1}{\mathcal{N}} \Psi_t(R_0) G(R_0, R_1, d\tau) \ldots \times G(R_{M-1}, R_M, d\tau) \Psi_t(R_M). \tag{B2}$$

Chosen a sufficiently long τ, a local operator $\hat{O}(R)$ can be evaluated on the ground state of the system by applying the operator in the center of the path integral,

$$\hat{O} G(R_{M/2}, R_{M/2+1}, d\tau) = \hat{O}(R_{M/2}) G(R_{M/2}, R_{M/2+1}, d\tau),$$
$$\langle \Psi_0 | \hat{O} | \Psi_0 \rangle = \int dR_0 \ldots dR_M\ \hat{O}(R_{M/2}) p(R_0, \ldots, R_M).$$

In PIGS, the expectation value in Eq. (B3) is evaluated with Monte Carlo methods using the Metropolis algorithm. The PIGS method is in principle exact, in the sense that the results are independent[32] of Ψ_t and systematic errors may be reduced below the statistical uncertainty.

A convergence test showed that a sufficiently small imaginary-time discretization is $6 * d\tau = \frac{1}{160}$ K^{-1}. The trial wave function that we have used is the product of a Jastrow-McMillan wave function and a Gaussian along the z direction,

$$\Psi_t = \exp\left[- \sum_{i<j=1}^{N} \left(\frac{b}{r_{ij}} \right)^m \right] \exp\left[- A \sum_{i=1}^{N} (z_0 - z_i)^2 \right], \tag{B3}$$

where N is the particle number and $r_{ij} = |\vec{r}_i - \vec{r}_j|$ is the distance between two atoms labeled i and j. The Jastrow parameters are $b = 2.84$ Å and $m = 5$. The Gaussian along the z direction (i.e., the direction perpendicular to the substrate plane) was used only far away from the layer promotion density; its parameters have been obtained with a fit of the density along the z direction: For GF $A = 5.6$ Å^{-2} and $z_0 = 3.72$ Å; for GH $A = 3.0$ Å^{-2} and $z_0 = 3.85$ Å. At high densities, where the probability to occupy the second layer is not negligible, a Jastrow wave function has been used,

$$\Psi_t^{hd} = \exp\left[- \sum_{i<j=1}^{N} \left(\frac{b}{r_{ij}} \right)^m \right]. \tag{B4}$$

With these trial wave functions, we allowed a $\Delta\tau = 0.15$ K^{-1} imaginary-time projection before computing the ground-state expectation values. The total imaginary time sampled in our calculations was $\tau = 0.4$ K^{-1}. The value of τ has been chosen following a convergence test of the total energy versus the imaginary-time projection.

For the finite-temperature simulations we used the path-integral Monte Carlo (PIMC) method[33] in the canonical ensemble, with an eight-order multiple product expansion of the propagator. These calculations have been employed in order to obtain an estimation of the superfluid density. Due to the computational complexity of PIMC especially at low

temperatures (i.e., 0.5 K), the imaginary-time discretization that was used is $6 * d\tau = \frac{1}{40}$ K^{-1}.

The worm algorithm[34] was used at both finite and zero temperature respectively for the sampling of the permutations and the computation of the one-body density matrix that has been obtained from the distribution function (B2) upon breaking up one of the paths.[31] The computations required on average 10^5 Monte Carlo steps; the heaviest computations were those made for the superfluid fraction at zero temperature and required approximately 10^6 Monte Carlo steps.

[1] S. Sachdev, Nat. Phys. **4**, 173 (2008); I. Bloch, J. Dalibard, and W. Zwerger, Rev. Mod. Phys. **80**, 885 (2008).

[2] R. G. Melko, A. Paramekanti, A. A. Burkov, A. Vishwanath, D. N. Sheng, and L. Balents, Phys. Rev. Lett. **95**, 127207 (2005); E. Edlund, O. Lindgren, and M. N. Jacobi, *ibid.* **107**, 085503 (2011).

[3] Sec. 6.1 of L. W. Brunch, M. W. Cole, and E. Zaremba, *Physical Adsorption: Forces and Phenomena* (Dover Publishing, Mineola, NY, 2007).

[4] Y. Shibayama, H. Fukuyama, and K. Shirahama, J. Phys: Conf. Series **150**, 032096 (2009).

[5] H. Fukuyama, J. Phys. Soc. Jpn. **77**, 111013 (2008).

[6] M. W. Cole, D. R. Frankl, and D. L. Goodstein, Rev. Mod. Phys. **53**, 199 (1981); L. W. Bruch, M. W. Cole, and H. Y. Kim, J. Phys.: Condens. Matter **22**, 304001 (2010).

[7] M. C. Gordillo and J. Boronat, Phys. Rev. Lett. **102**, 085303 (2009).

[8] Y. Kwon and D. M. Ceperley, Phys. Rev. B **85**, 224501 (2012).

[9] R. R. Nain *et al.*, Small **6**, 2877 (2010); R. Zobril *et al.*, *ibid.* **6**, 2885 (2010).

[10] J. O. Sofo, A. S. Chaudhari, and G. D. Barber, Phys. Rev. B **75**, 153401 (2007); D. C. Elias *et al.*, Science **323**, 610 (2009).

[11] M. D. Miller and L. H. Nosanow, J. Low Temp. Phys. **32**, 145 (1978).

[12] L. Reatto, M. Nava, D. E. Galli, C. Billman, J. O. Sofo, and M. W. Cole, arXiv:1204.3061 [J. Phys: Conf. Series (to be published)].

[13] M. J. Stott and E. Zaremba, Phys. Rev. B **22**, 1564 (1980); M. W. Cole and F. Toigo, *ibid.* **31**, 727 (1985).

[14] G. Vidali, M. W. Cole, and C. Schwartz, Surf. Sci. **87**, L273 (1979).

[15] K. T. Tang and J. P. Toennies, J. Chem. Phys. **80**, 3726 (1984).

[16] W. E. Carlos and M. W. Cole, Phys. Rev. B **21**, 3713 (1980).

[17] A. Sarsa, K. E. Schmidt, and W. R. Magro, J. Chem. Phys. **113**, 1366 (2000).

[18] E. Vitali, M. Rossi, L. Reatto, and D. E. Galli, Phys. Rev. B **82**, 174510 (2010).

[19] R. A. Aziz, V. P. S. Nain, J. S. Carley, W. L. Taylor, and G. T. McConville, J. Chem. Phys. **70**, 4330 (1979).

[20] P. A. Whitlock, G. V. Chester, and M. H. Kalos, Phys. Rev. B **38**, 2418 (1988).

[21] P. A. Whitlock, G. V. Chester, and B. Krishnamachari, Phys. Rev. B **58**, 8704 (1998).

[22] M. E. Pierce and E. Manousakis, Phys. Rev. Lett. **83**, 5314 (1999).

[23] A. J. Leggett, J. Stat. Phys. **93**, 927 (1998); K. H. Kim and W. F. Saam, Phys. Rev. B **48**, 13735 (1993).

[24] S. Zhang, N. Kawashima, J. Carlson, and J. E. Gubernatis, Phys. Rev. Lett. **74**, 1500 (1995).

[25] D. M. Ceperley, Rev. Mod. Phys. **67**, 279 (1995).

[26] M. Greiner, O. Mandel, T. W. Hansch, and I. Bloch, Nat. Phys. **415**, 39 (2002).

[27] M. Nava, A. Motta, D. E. Galli, E. Vitali, and S. Moroni, Phys. Rev. B **85**, 184401 (2012).

[28] G. Carleo, S. Moroni, F. Becca, and S. Baroni, Phys. Rev. B **83**, 060411 (2011).

[29] M. Rossi, E. Vitali, L. Reatto, and D. E. Galli, Phys. Rev. B **85**, 014525 (2012).

[30] M. Nava, D. E. Galli, M. W. Cole, and L. Reatto, J. Low Temp. Phys., doi: 10.1007/s10909-012-0770-9 (2012).

[31] R. E. Zillich, J. M Mayrhofer, and S. A Chin, J. Chem. Phys. **132**, 044103 (2010).

[32] M. Rossi, M. Nava, L. Reatto, and D. E Galli, J. Chem. Phys. **131**, 154108 (2009).

[33] D. M. Ceperley, Rev. Mod. Phys. **67**, 279 (1995).

[34] M. Boninsegni, N. V. Prokof'ev, and B. V. Svistunov, Phys. Rev. E **74**, 036701 (2006).